Delft University of Technology

Dynamical modelling of NASA's ACS3 solar sail mission

Minervino Amodio, Andrea; Visser, Pieter; Heiligers, Jeannette

DOI
10.1016/j.ast.2025.110146

Publication date
2025

Document Version
Final published version

Published in
Aerospace Science and Technology

Aerospace Science and Technology 161 (2025) 110146

Contents lists available at ScienceDirect

Aerospace Science and Technology

journal homepage: www.elsevier.com/locate/aescte

Dynamical modelling of NASA's ACS3 solar sail mission

Andrea Minervino Amodio *, Pieter Visser, Jeannette Heiligers

Delft University of Technology, Faculty of Aerospace Engineering, Section of Astrodynamics and Space Missions, Kluyverweg 1, Delft, 2629 HS, The Netherlands

ARTICLE INFO

Communicated by Mehdi Ghoreyshi

Keywords:
Solar sail
Solar radiation pressure
Planetary radiation pressure
Sensitivity analysis
Orbit determination

ABSTRACT

NASA's ACS3 mission aims to be the first Earth-bound solar sail to execute calibration steering laws for in-orbit estimation of solar-sail acceleration parameters. To maximise the mission's scientific return, this study identifies the physical effects to include in the dynamical model, the solar-sail acceleration parameters observable from flight data, and the uncertainties to consider during the orbit determination process. The sensitivity of the solar-sail dynamics to perturbations, model uncertainties, and sail-attitude errors is investigated by 1) comparing a reference orbit with modified orbits, each altered in a single dynamical aspect, and 2) evaluating the accuracy of modified models in reconstructing the reference orbit through iterative initial state adjustments.

For the one-sigma 10-meter observation noise level of the ACS3 mission and a seven-day arc, results indicate that higher-order lunar perturbations, planetary third-body effects, and relativistic corrections can be omitted from the dynamical model. Additionally, the geopotential expansion may be limited to degree and order 32. In contrast, the dynamics should include the effects of solid Earth tides, account for the instantaneous Sun-sailcraft distance in the solar radiation pressure model, and assume imperfect reflection from the sail surface in the solar and planetary radiation pressure models. Furthermore, the analysis reveals varying levels of observability for the sail optical coefficients, with frontside reflectivity and specularity showing the strongest influence on the solar-sail dynamics. Finally, systematic attitude errors and uncertainties in atmospheric density and accommodation coefficients are the most challenging factors to absorb through initial state adjustment, potentially complicating the estimation of solar-sail acceleration parameters.

1. Introduction

Solar sailing is a propulsion system that uses solar radiation pressure (SRP) exerted on a thin, lightweight sail to generate thrust. This propellantless technology has attracted significant interest for a wide range of applications, spanning Earth-bound, interplanetary, and even interstellar missions [1,2]. Over the past decade, several technology demonstrator missions have advanced solar-sail technology. These include IKAROS by JAXA (2010), NanoSail-D2 by NASA (2010), and LightSail 1 and 2 by The Planetary Society (2015, 2019) [3,4]. Continuing to push the boundaries of this technology, NASA launched the Advanced Composite Solar Sail System (ACS3) mission on April 23, 2024 [5].

ACS3 serves as a sail-deployment demonstrator and aims to be the first sailcraft to execute calibration steering laws. These steering laws are attitude control profiles designed to isolate the different contributions that make up the solar-sail acceleration, particularly SRP, planetary radiation pressure (PRP), and aerodynamic effects. Through the in-orbit estimation of parameters governing these accelerations, the calibration laws facilitate the acquisition of valuable data for improving current solar-sail acceleration models. This improvement is particularly crucial for solar sails in Earth-bound orbits, where factors such as albedo, blackbody radiation, solar-cycle variability, and sail degradation have yet to be thoroughly investigated.

Despite extensive research on solar-sail behaviour around Earth, the majority of studies focus on trajectory optimisation in simplified dynamical environments. For instance, Carzana et al. [6] examined the effects of solar-cycle variability on locally optimal control laws for ideal sails, considering atmospheric drag and Earth's oblateness while neglecting PRP acceleration. Other works developed optimal steering laws for ideal solar sails under blackbody and albedo radiation pressure but overlooked the effects of higher-order Earth gravity, third-body perturbations, and atmospheric drag [7,8]. Studies that employed a more realistic optical flat-sail model generally restrict their dynamics to gravitational perturbations only [9–11]. Recent literature [12–14] has also examined various sail deformation factors: surface roughness, creases from folding and deployment, crinkles from mechanical processing,

* Corresponding author.
E-mail addresses: a.minervinoamodio@tudelft.nl (A. Minervino Amodio), p.n.a.m.visser@tudelft.nl (P. Visser), m.j.heiligers@tudelft.nl (J. Heiligers).

https://doi.org/10.1016/j.ast.2025.110146
Received 10 December 2024; Received in revised form 13 March 2025; Accepted 14 March 2025

Available online 18 March 2025

wrinkles from localised compressive stress, and billowing from manufacturing errors, thermal gradients, or incorrect boom deployment. These studies demonstrate that deviations from a flat-plate geometry can affect both the magnitude and direction of the sail acceleration, yet without addressing their impact on the solar-sail orbital dynamics in perturbed environments. This fragmented approach, while valuable for isolating individual effects, falls short of providing a comprehensive understanding of solar-sail dynamics in the highly perturbed near-Earth environment. The present study addresses this gap by investigating the sensitivity of the ACS3 solar-sail dynamics to various perturbations, model uncertainties, and sail-attitude errors. While modelling the actual geometry of a deployed sail is beyond the scope of this work, the sensitivity analysis addresses factors that can mimic deviations from the flat-plate behaviour and can provide insights into their effects on the sail's orbital evolution. This sensitivity analysis is also the necessary first step in the overall investigation of the ACS3 mission, as it will directly inform future studies exploring the capabilities of calibration steering laws to estimate solar-sail acceleration parameters.

The behaviour of the solar-sail dynamics is analysed over a seven-day window, representing the maximum flight time allocated to each candidate calibration steering law in ACS3 mission planning. One of these laws, referred to as backside nadir pointing, corresponds to ACS3's standby mode. This calibration law orients the sail with its back facing Earth and perpendicular to the orbit radial direction, ensuring optimal contact with ground stations since the antennas are placed on the back of the sailcraft bus. Given its guaranteed implementation in the mission, the backside nadir pointing calibration steering law serves as the nominal attitude profile examined in this study.

The sensitivity analysis relies on two complementary approaches. In the first, a high-fidelity reference orbit, propagated using a reference acceleration model, is compared with so-called *modified orbits*. These modified orbits are propagated using acceleration models that deviate from the reference one in a single aspect. The differences between the reference orbit and each modified orbit are referred to as pre-fit residuals. The second approach simulates ideal three-dimensional position observations using the reference acceleration model. These observations, combined with each modified acceleration model, feed into a least-squares orbit determination algorithm. This algorithm iteratively adjusts the sailcraft's initial state to compute a new, fitted orbit that minimises deviations from the reference orbit. These deviations are defined as post-fit residuals. By simulating the sailcraft dynamics under diverse conditions and analysing the resulting pre-fit and post-fit residuals, this work helps to determine the key factors affecting the solar-sail orbital evolution and evaluate the robustness of the dynamical model to uncertainties and errors. Specifically, the sensitivity analysis identifies potential model simplifications having a negligible impact on the accuracy of the orbit solution, highlights uncertainties requiring careful consideration during orbit determination, and indicates the solar-sail acceleration parameters best suited for estimation from flight data. To the best of the authors' knowledge, this study represents the first comprehensive sensitivity analysis of its kind applied specifically to solar-sail dynamics, offering invaluable insights for ACS3 mission analysis and laying the groundwork for improved, flight-data-driven models that can more accurately predict solar-sail trajectories and performance.

The paper is structured as follows: Section 2 provides a description of the dynamical models governing the solar-sail dynamics. Section 3 presents the two-step approach employed for the sensitivity analysis, followed by Section 4, which describes the simulation setup used to generate the results. Section 5 provides the results of the sensitivity analysis, along with a discussion of their implications for the ACS3 mission. Finally, Section 6 offers a summary of the overall conclusions.

2. Dynamical models

The dynamics of ACS3 are described in an Earth-centred inertial (ECI) reference frame $I(\hat{\boldsymbol{x}}_I, \hat{\boldsymbol{y}}_I, \hat{\boldsymbol{z}}_I)$. In this frame, the $\hat{\boldsymbol{z}}_I$-axis points north in the direction of Earth's rotation axis, the $\hat{\boldsymbol{x}}_I\hat{\boldsymbol{y}}_I$-plane coincides with Earth's equatorial plane, the $\hat{\boldsymbol{x}}_I$-axis aligns with the mean vernal equinox at January 1st, 2000, and the $\hat{\boldsymbol{y}}_I$-axis completes the right-handed system. Unless explicitly stated otherwise, all vectors and equations in this paper are expressed in the ECI frame. The equation of motion is given by:

$$\ddot{\boldsymbol{r}} = \boldsymbol{a}_{grav} + \boldsymbol{a}_{aero} + \boldsymbol{a}_{SRP} + \boldsymbol{a}_{PRP} \tag{1}$$

where $\boldsymbol{r}$ denotes the sailcraft position vector, and the overhead dot notation indicates differentiation with respect to time. The term $\boldsymbol{a}_{grav}$ represents the acceleration due to gravitational interactions of N bodies, $\boldsymbol{a}_{aero}$ denotes the aerodynamic acceleration, and $\boldsymbol{a}_{SRP}$ and $\boldsymbol{a}_{PRP}$ represent the accelerations due to solar radiation pressure and planetary radiation pressure, respectively. The following subsections detail the models used to characterise each of these acceleration components.

2.1. Gravitational acceleration

To accurately model the gravitational acceleration, $\boldsymbol{a}_{grav}$, the gravitational potentials of relevant bodies need to be defined. This potential-based approach captures central body and third-body interactions, addressing both point mass and extended body characteristics, as well as tidal perturbations, while relativistic effects are incorporated as additional corrective terms.

The gravitational potential of body i, evaluated at point j, $U_i(\boldsymbol{r}_j)$, can be decomposed into a point mass contribution $U_{\bar{i}}(\boldsymbol{r}_j)$, and an extended body contribution $U_{\hat{i}}(\boldsymbol{r}_j)$:

$$U_i(\boldsymbol{r}_j) = U_{\bar{i}}(\boldsymbol{r}_j) + U_{\hat{i}}(\boldsymbol{r}_j) \tag{2}$$

The potential of the point-mass gravity field is given by:

$$U_{\bar{i}}(\boldsymbol{r}_j) = \frac{\mu_i}{\boldsymbol{r}_{ij}} \tag{3}$$

where μ_i is the gravitational parameter of body i, and $\boldsymbol{r}_{ij} = \boldsymbol{r}_j - \boldsymbol{r}_i$ represents the position vector from the centre of mass of body i to point j.

The extended body contribution, which accounts for any deviation in the spherical mass distribution of body i, is expressed using spherical harmonics [15]:

$$U_{\hat{i}}(\boldsymbol{r}_j) = \sum_{l=1}^{\infty}\sum_{m=0}^{l} U_{i,lm}(\boldsymbol{r}_{ij}) \tag{4}$$

$$U_{i,lm}(\boldsymbol{r}_{ij}) = \mu_i \frac{R_{e,i}^l}{r_{ij}^{l+1}} \bar{P}_{lm}(\sin\phi_{ij}) \left(\bar{C}_{lm}^{(i)}\cos m\lambda_{ij} + \bar{S}_{lm}^{(i)}\sin m\lambda_{ij}\right) \tag{5}$$

Here, ϕ_{ij} and λ_{ij} represent the latitude and longitude of point j in a frame centred and fixed to body i, $R_{e,i}$ is the reference radius of the spherical harmonic expansion (typically, the equatorial radius), $\bar{P}_{lm}$ is the normalised associated Legendre polynomial of degree l and order m, and $\bar{C}_{lm}^{(i)}$ and $\bar{S}_{lm}^{(i)}$ are the fully-normalised spherical harmonic coefficients of body i, expressing its mass distribution. In general, these coefficients change over time due to any number of tide-raising point masses q, with the main variation computed as [16]:

$$\Delta\bar{C}_{lm}^{(i)} - i\Delta\bar{S}_{lm}^{(i)} = \frac{1}{2l+1}\sum_q k_{lm}\frac{\mu_q}{\mu_i}\left(\frac{R_{e,i}}{r_{iq}}\right)^{l+1}\bar{P}_{lm}(\sin\phi_{iq})\, e^{-im\lambda_{iq}} \tag{6}$$

where μ_q is the gravitational parameter of the tide-raising body q, and k_{lm} is the tidal Love number at degree l and order m.

The total gravitational acceleration acting on the sailcraft s, as exerted by N extended bodies, denoted with $i = 0, \ldots, N$, with respect to the central body $i = 0$, is expressed as:

$$\boldsymbol{a}_{grav} = \boldsymbol{a}_{0,s}\Big|_0 + \sum_{i=1}^{N}\boldsymbol{a}_{i,s}\Big|_0 \tag{7}$$

where $\boldsymbol{a}_{0,s}$ represents the gravitational acceleration acting on the sailcraft due to the central body 0, and $\boldsymbol{a}_{i,s}$ denotes the so-called third-body perturbation acting on the sailcraft due to body i. The notation "$\big|_0$" indicates that the acceleration components are expressed in the frame originating at the centre of mass of the central body, which in this paper corresponds to $I(\hat{\boldsymbol{x}}_I, \hat{\boldsymbol{y}}_I, \hat{\boldsymbol{z}}_I)$.

Using the gradient of the gravitational potential (Eqs. (2)-(4)), the first term on the right-hand side of Eq. (7), the acceleration due to the central body, is computed as:

$$\boldsymbol{a}_{0,s}\Big|_0 = \nabla U_0(\boldsymbol{r}_{0s}) = -\mu_0 \frac{\hat{\boldsymbol{r}}_{0s}}{\|\boldsymbol{r}_{0s}\|^2} + \nabla U_{\hat{0}}(\boldsymbol{r}_{0s}) \tag{8}$$

The second term on the right-hand side of Eq. (7), the third-body acceleration, is calculated as the difference between the gravitational attraction of body i on the sailcraft and that exerted by body i on the central body:

$$\boldsymbol{a}_{i,s}\Big|_0 = \nabla U_i(\boldsymbol{r}_{is}) - \nabla U_i(\boldsymbol{r}_{i0}) \tag{9}$$

Expanding Eq. (9) using the previously defined potentials yields:

$$\boldsymbol{a}_{i,s}\Big|_0 = \left(-\mu_i \frac{\hat{\boldsymbol{r}}_{is}}{\|\boldsymbol{r}_{is}\|^2} + \nabla U_{\hat{i}}(\boldsymbol{r}_{is})\right) - \left(-\mu_i \frac{\hat{\boldsymbol{r}}_{i0}}{\|\boldsymbol{r}_{i0}\|^2} + \underbrace{\nabla U_{\hat{i}}(\boldsymbol{r}_{i0}) - \nabla U_{\hat{0}}(\boldsymbol{r}_{0i})}_{\text{indirect oblateness}}\right) \tag{10}$$

The last two terms, collectively referred to as *indirect oblateness* [17], account for the gravitational attraction between the extended body i and the point-mass 0, and the gravitational attraction between the extended body 0 and the point-mass i, respectively.

The gravitational accelerations described by the previous equations are based on a Newtonian model of gravity. While the total relativistic perturbation includes several corrective terms, for low Earth orbit (LEO) applications not specifically related to geodesy or tests of relativity, only the Schwarzschild correction is typically considered [18]. This perturbation, approximately on the order of 10^9 smaller than the main Newtonian acceleration, provides a first-order correction to the central body point-mass acceleration given by Eq. (8) and is included in the model as an indication of the magnitude of relativistic effects [16]:

$$\Delta\boldsymbol{a}_{0,s}\Big|_0 = \frac{\mu_0}{c^2 r_{0s}^3}\left[\left(4\frac{\mu_0}{r_{0s}} - \dot{\boldsymbol{r}}_{0s}\cdot\dot{\boldsymbol{r}}_{0s}\right)\boldsymbol{r}_{0s} + 4(\boldsymbol{r}_{0s}\cdot\dot{\boldsymbol{r}}_{0s})\dot{\boldsymbol{r}}_{0s}\right] \tag{11}$$

where $c = 299792458$ m/s is the speed of light in vacuum [19].

2.2. Aerodynamic acceleration

The aerodynamic acceleration is defined in the aerodynamic frame $A(\hat{\boldsymbol{x}}_A, \hat{\boldsymbol{y}}_A, \hat{\boldsymbol{z}}_A)$. This frame has its origin at the centre of mass of the sailcraft, with the $\hat{\boldsymbol{x}}_A$-axis aligned along the sailcraft velocity vector relative to the atmosphere, the $\hat{\boldsymbol{z}}_A$-axis opposite to the direction of the lift acceleration, and the $\hat{\boldsymbol{y}}_A$-axis completing the right-handed coordinate system. The aerodynamic acceleration is expressed in frame A as [20]:

$$\boldsymbol{a}_{aero}\Big|_A = -\begin{pmatrix} C_D \\ C_S \\ C_L \end{pmatrix} \frac{1}{2}\rho v^2 \frac{S_{ref}}{m} \tag{12}$$

where C_D, C_S, and C_L are the drag, side force, and lift coefficients, respectively, v is the sailcraft velocity relative to the atmosphere, ρ is the atmospheric density, S_{ref} is the aerodynamic reference area, and m is the sailcraft mass.

In LEO, the low atmospheric density leads to a free molecular flow regime, where Gas-Surface Interactions (GSI) become predominant in determining the aerodynamic coefficients. The nature of these interactions varies due to several factors, including the spacecraft speed relative to the atmosphere, the spacecraft surface temperature, the atmospheric translational temperature, and the atmospheric composition [21]. This paper adopts the Schaaf and Chambre (SC) model for describing these interactions [22]. The SC model can simulate various types of reflection for the surface-interacting particles – specular, diffuse, and quasi-specular – through momentum accommodation coefficients, making it versatile for different LEO conditions. In contrast, other models, such as Sentman's and Schamberg's, have limitations. Sentman's model, which assumes diffuse reflection, may not accurately represent particle behaviour above ~500 km where reflection characteristics are less certain [23]. Schamberg's model assumes hyperthermal flow, where the sailcraft velocity is much larger than the thermal velocity of the atmospheric particles, which becomes less accurate at higher altitudes [24].

Considering the sail's relatively large area in relation to the main spacecraft body, the sailcraft can be modelled as a flat plate. This simplification allows using Storch's closed-form solutions for aerodynamic coefficients of basic geometries under the SC model [25]. Then, in the aerodynamic reference frame, the aerodynamic coefficients of a flat plate in free-molecular flow can be expressed as:

$$\begin{aligned} C_D\Big|_A = &\frac{\sigma_n}{s}\sqrt{\frac{\pi T_s}{T_\infty}}n_x^2 + \frac{2}{s\sqrt{\pi}}\left[(2-\sigma_n)n_x^2 + \sigma_t\left(n_y^2+n_z^2\right)\right]e^{-s^2 n_x^2} + \\ &+ 2\left[(2-\sigma_n)\left(n_x^2 + \frac{1}{2s^2}\right) + \sigma_t\left(n_y^2+n_z^2\right)\right]\|n_x\|\,\mathrm{erf}\big(s\|n_x\|\big) \end{aligned} \tag{13}$$

$$\begin{aligned} \begin{pmatrix} C_S \\ C_L \end{pmatrix}\Bigg|_A = &\,2\left[\frac{2-\sigma_n-\sigma_t}{s\sqrt{\pi}}e^{-s^2 n_x^2} + \frac{\sigma_n}{2s}\sqrt{\frac{\pi T_s}{T_\infty}}\right]n_x\begin{pmatrix} n_y \\ n_z \end{pmatrix} \\ &+ \left[\frac{2-\sigma_n}{s^2} + 2\left(2-\sigma_n-\sigma_t\right)n_x^2\right]\mathrm{erf}\big(s\,n_x\big)\begin{pmatrix} n_y \\ n_z \end{pmatrix} \end{aligned} \tag{14}$$

In these equations, $\hat{\boldsymbol{n}}\Big|_A = \left(n_x, n_y, n_z\right)$ denotes the sail normal direction expressed in the aerodynamic frame, σ_n and σ_t represent the normal and tangential momentum accommodation coefficients, respectively, T_s is the temperature of the sail surface, T_∞ is the atmospheric translational temperature, and s is defined as the ratio of the sailcraft inertial velocity to the atmospheric particle average thermal velocity v_a. The average thermal velocity v_a is calculated using the Maxwell-Boltzmann distribution [26]:

$$v_a = \sqrt{\frac{2k_B T_\infty}{m_a}} \tag{15}$$

where $k_B = 1.380649 \times 10^{-23}$ K/J is the Boltzmann constant, and m_a is the mean molecular mass of the atmospheric particles.

To express the aerodynamic acceleration in frame I, the intermediate body frame $B(\hat{\boldsymbol{x}}_B, \hat{\boldsymbol{y}}_B, \hat{\boldsymbol{z}}_B)$ is introduced. This frame has its origin at the centre of mass of the sailcraft, with the $\hat{\boldsymbol{z}}_B$-axis directed normal to the sail, pointing out from the front of the sail, the $\hat{\boldsymbol{x}}_B\hat{\boldsymbol{y}}_B$-plane coinciding with the plane of the sail, the $\hat{\boldsymbol{x}}_B$-axis directed parallel to one edge of the sail, and the $\hat{\boldsymbol{y}}_B$-axis completing the right-handed system. Fig. 1 illustrates the transformation from frame I to frame B, achieved through three successive rotations: a rotation about the $\hat{\boldsymbol{z}}_I$-axis, followed by a rotation about the (local) $\hat{\boldsymbol{y}}_I$-axis, and concluded by a rotation about the $\hat{\boldsymbol{x}}_B$-axis. The angles associated with these rotations are the yaw ψ, pitch θ, and roll ϕ angles, respectively. These Euler angles express the attitude of the sailcraft with respect to the inertial frame. Fig. 2 shows the transformation from frame B to frame A, requiring two consecutive rotations: a rotation about the $\hat{\boldsymbol{y}}_B$ axis over an angle equal to the negative angle of attack $-\alpha$, followed by a rotation about the $\hat{\boldsymbol{z}}_A$ axis over an angle equal to the positive angle of sideslip β.

The acceleration in frame I can then be expressed as:

$$\boldsymbol{a}_{aero}\Big|_I = \boldsymbol{C}_{I,B}\,\boldsymbol{C}_{B,A}\,\boldsymbol{a}_{aero}\Big|_A \tag{16}$$

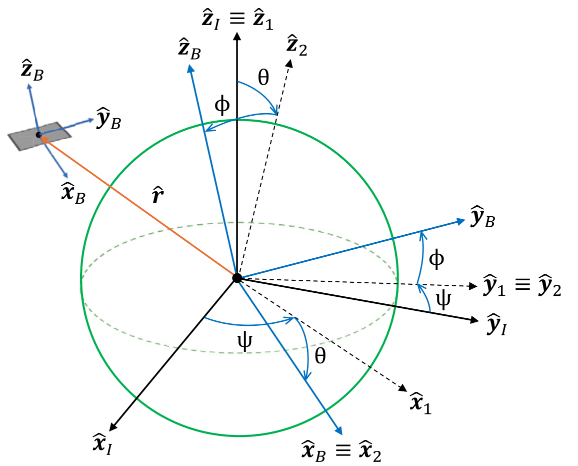

Fig. 1. Schematic representation of the inertial (index I) and body (index B) frames.

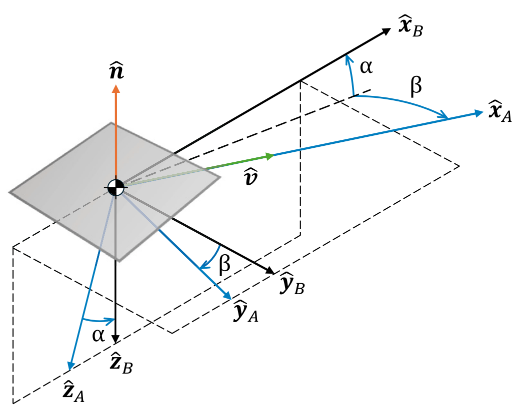

Fig. 2. Schematic representation of the body (index B) and aerodynamic (index A) frames.

where $\boldsymbol{C}_{B,A} = \boldsymbol{R}_{\hat{y}_B}(\alpha)\,\boldsymbol{R}_{\hat{z}_A}(-\beta)$ is the rotation matrix from the aerodynamic frame to the body frame, and $\boldsymbol{C}_{I,B} = \boldsymbol{R}_{\hat{z}_I}(-\psi)\,\boldsymbol{R}_{\hat{y}_I}(-\theta)\,\boldsymbol{R}_{\hat{x}_B}(-\phi)$ is the rotation matrix from the body frame to the inertial frame.

2.3. Solar radiation pressure acceleration

The SRP acceleration model employed in this study is based on the flat-sail optical SRP acceleration model of McInnes [27], but extended to scenarios where either side of the sail can be illuminated. This extension is particularly relevant for the ACS3 mission, because its standby attitude mode results in sunlight exposure of the back of the sail.

The SRP acceleration is defined as:

$$\boldsymbol{a}_{SRP} = \nu \frac{2S_{\oplus}}{c}\left(\frac{1\text{AU}}{u}\right)^2 \frac{A}{m}\left(\hat{\boldsymbol{u}}\cdot\hat{\boldsymbol{n}}_u\right)\left\{b_1\hat{\boldsymbol{u}} + \left[b_2\left(\hat{\boldsymbol{u}}\cdot\hat{\boldsymbol{n}}_u\right) + b_3\right]\hat{\boldsymbol{n}}_u\right\} \tag{17}$$

with ν the Earth shadow function computed using the conical shadow model [15], $S_{\oplus}$ the solar irradiance at one astronomical unit (AU) from the Sun, A the sail area, and $\hat{\boldsymbol{u}} = \boldsymbol{u}/u$ the instantaneous Sun-to-sailcraft unit vector. The sail normal direction without any positive component towards the Sun, $\hat{\boldsymbol{n}}_u$, is given by:

$$\hat{\boldsymbol{n}}_u = \text{sgn}(\hat{\boldsymbol{u}}\cdot\hat{\boldsymbol{n}})\,\hat{\boldsymbol{n}}$$

where $\hat{\boldsymbol{n}}$ is the sail normal direction pointing out from the back of the sail.

The parameters b_1, b_2, and b_3 are defined as:

$$b_1 = \frac{1}{2}(1-\tilde{r}_{sl}\,\tilde{s}_{sl}) \qquad b_2 = \tilde{r}_{sl}\,\tilde{s}_{sl}$$

$$b_3 = \frac{1}{2}\left(B_{sl}\,(1-\tilde{s}_{sl})\,\tilde{r}_{sl} + \text{sgn}(\hat{\boldsymbol{u}}\cdot\hat{\boldsymbol{n}})\,(1-\tilde{r}_{sl})\,\frac{\varepsilon_f B_f - \varepsilon_b B_b}{\varepsilon_f + \varepsilon_b}\right)$$

where $\tilde{r}$, $\tilde{s}$, B, and ε denote the reflectivity, specularity, non-Lambertian coefficient, and emissivity of the sail, respectively. The subscripts *"f"*, *"b"*, and *"sl"* indicate whether the optical coefficients correspond to the front, back, or sunlit side of the sail. Depending on the attitude of the sail, the sunlit optical coefficients match those of either the front or back of the sail:

$$\tilde{r}_{sl},\ \tilde{s}_{sl},\ B_{sl} = \begin{cases} \tilde{r}_f,\ \tilde{s}_f,\ B_f & \text{if } \text{sgn}(\hat{\boldsymbol{u}}\cdot\hat{\boldsymbol{n}}) = 1 \\ \tilde{r}_b,\ \tilde{s}_b,\ B_b & \text{otherwise} \end{cases}$$

2.4. Planetary radiation pressure acceleration

The PRP acceleration model employed in this paper is the spherical optical PRP acceleration model presented in Carzana et al. [28]. This model accounts for the albedo radiation pressure (ARP) and blackbody radiation pressure (BBRP) accelerations exerted on the sailcraft due to sunlight reflected by the Earth and thermal radiation emitted by the Earth, respectively, while considering the sail optical properties. The total PRP acceleration can be expressed as the sum of these two components:

$$\boldsymbol{a}_{PRP} = \boldsymbol{a}_{BBRP} + \boldsymbol{a}_{ARP} \tag{18}$$

Both the ARP and BBRP components share a similar mathematical structure, which can be expressed in the following general form:

$$\begin{aligned}\boldsymbol{a}_p = \frac{S_p}{c}\frac{A}{m}\Bigg\{ &\frac{2}{3}\left[\left(1+\tilde{r}_{in}\tilde{s}_{in}\right)G_{FNS,in} - \left(1+\tilde{r}_{out}\tilde{s}_{out}\right)G_{FNS,out}\right]\text{sgn}(\hat{\boldsymbol{r}}\cdot\hat{\boldsymbol{n}})\,\hat{\boldsymbol{n}} \\ &+ \left[\left(1-\tilde{s}_{in}\right)\tilde{r}_{in}B_{in}\,G_{FND,in} - \left(1-\tilde{s}_{out}\right)\tilde{r}_{out}B_{out}\,G_{FND,out}\right]\text{sgn}(\hat{\boldsymbol{r}}\cdot\hat{\boldsymbol{n}})\,\hat{\boldsymbol{n}} \\ &+ \frac{\varepsilon_f B_f - \varepsilon_b B_b}{\varepsilon_f + \varepsilon_b}\left[\left(1-\tilde{r}_{in}\right)G_{FND,in} + \left(1-\tilde{r}_{out}\right)G_{FND,out}\right]\hat{\boldsymbol{n}} \\ &+ \frac{2}{3\pi}\left[\left(1-\tilde{r}_{in}\tilde{s}_{in}\right)G_{FT,in} + \left(1-\tilde{r}_{out}\tilde{s}_{out}\right)G_{FT,out}\right]\hat{\boldsymbol{d}}\Bigg\}\end{aligned} \tag{19}$$

In this equation, the geometrical factors G_{FNS}, G_{FND}, G_{FT} represent the normal specular, normal diffusive, and transversal geometrical factor, respectively, and depend on the instantaneous Earth-sail geometrical configuration. The subscripts *"in"* and *"out"* indicate if the optical coefficients and geometrical factor refer to the inward or outward side of the sail with respect to Earth. The sail normal direction $\hat{\boldsymbol{n}}$ is defined the same as for the SRP model. The sailcraft radial direction $\hat{\boldsymbol{r}}$ is the unit vector from the centre of the Earth to the sailcraft, and the transversal direction $\hat{\boldsymbol{d}}$ is defined as:

$$\hat{\boldsymbol{d}} = \hat{\boldsymbol{n}} \times \frac{\hat{\boldsymbol{r}}\times\hat{\boldsymbol{n}}}{\|\hat{\boldsymbol{r}}\times\hat{\boldsymbol{n}}\|} \tag{20}$$

The subscript p in Eq. (19) serves to differentiate between the two types of radiation pressure, indicating that the sail reflectivity $\tilde{r}$ and the incident radiation flux S are radiation-source specific. For ARP and BBRP, the reflectivity pertains to the visible and infrared spectrum, respectively. The fluxes for albedo and blackbody radiation are defined as [29]:

$$S_{AR} = S_{\oplus}\left[\Lambda_{eq} + \left(\Lambda_{pol} - \Lambda_{eq}\right)L_F\right]\Phi \tag{21}$$

$$S_{BBR} = S_{BBR,eq} + \left(S_{BBR,pol} - S_{BBR,eq}\right)L_F \tag{22}$$

Here, Λ_{eq} and Λ_{pol} are the reference albedo coefficients at the equator and poles, respectively, L_F is the latitudinal factor, Φ is the albedo phase function, and $S_{BBR,eq}$ and $S_{BBR,pol}$ are the reference blackbody radiation fluxes at the equator and the poles, respectively.

For a comprehensive treatment of the model, including detailed definitions of the geometrical factors, albedo phase function, and latitudinal factor, the reader is referred to Carzana et al. [28,29].

3. Methodology

This paper evaluates the sensitivity of the ACS3 orbit to various perturbations, model uncertainties, and sail-attitude errors, providing insights into the relative importance of different dynamical effects on the solar-sail behaviour. The methodology adopted here has been widely used in astrodynamics to investigate the impact of dynamical perturbations and modelling assumptions, with applications ranging from planetary moon dynamics to spacecraft orbit determination [30–33]. To present this methodology, it is helpful to first define the state vector, $\boldsymbol{x}$, which evolves over time, t, and is influenced by its initial state, $\boldsymbol{x}_0$, and by the acceleration model, $\boldsymbol{a}$, describing its dynamics:

$$\boldsymbol{x} = \boldsymbol{x}(t; \boldsymbol{x}_0, \boldsymbol{a}) \tag{23}$$

The sensitivity analysis is conducted using two complementary approaches, each offering distinct insights into the impact of perturbations and model uncertainties. The first approach involves propagating a reference orbit and a series of modified orbits, all originating from the same initial state. The reference orbit is propagated using a high-fidelity acceleration model incorporating all known perturbations with their nominal parameter values. Modified orbits are generated using acceleration models that deviate from the reference one in a single aspect, such as deactivating a particular perturbation, employing an alternative perturbation model, or altering specific perturbation parameters. This process causes the modified orbits to deviate from the reference one. These deviations, defined as pre-fit orbit residuals, $\Delta\boldsymbol{x}_{pre}$, are computed as:

$$\Delta\boldsymbol{x}_{pre}(t) = \boldsymbol{x}(t; \boldsymbol{x}_0, \boldsymbol{a}_{mod}) - \boldsymbol{x}(t; \boldsymbol{x}_0, \boldsymbol{a}_{ref}) \tag{24}$$

where $\boldsymbol{a}_{ref}$ and $\boldsymbol{a}_{mod}$ represent the reference and modified acceleration models, respectively. By assuming perfect knowledge of the orbital starting conditions, this approach quantifies the direct impact of each model modification on the accuracy of the propagated orbit and provides insight into how different perturbations and model uncertainties affect the trajectory over time.

The second approach evaluates model differences through an orbit determination process, determining how accurately the modified acceleration models can reproduce the reference orbit when adjusting the initial state. The analysis of whether and how model deviations are absorbed through initial state estimation – accounting for the real-world uncertainty in orbital starting conditions – provides insights into the observability of different perturbations and model parameters within the constraints of available knowledge.

To implement this approach, ideal three-dimensional position observations of ACS3 are simulated at times t_j as $\boldsymbol{x}(t_j, \boldsymbol{x}_0, \boldsymbol{a}_{ref})$ using the reference acceleration model. Based on ACS3 operational capabilities, these observations are simulated at regular intervals of 60 seconds across a seven-day window. This cadence is also sufficiently small to capture the effects of the model modifications analysed in this study, which have characteristic time scales longer than one minute. As the observations are assumed to be error-free, any mismatch post-convergence is solely due to differences in the dynamical model. A least-squares orbit determination algorithm is used with uniform observation weighting and without estimating any parameters of the acceleration model. The correction to the initial state vector, $\Delta\boldsymbol{x}_0$, is then obtained by minimising:

$$\min_{\Delta\boldsymbol{x}_0}\left(\sum_j \|\boldsymbol{x}(t_j; \boldsymbol{x}_0 + \Delta\boldsymbol{x}_0, \boldsymbol{a}_{mod}) - \boldsymbol{x}(t_j; \boldsymbol{x}_0, \boldsymbol{a}_{ref})\|^2\right) \tag{25}$$

Consequently, the post-fit orbit residuals are calculated as:

$$\Delta\boldsymbol{x}_{post}(t) = \boldsymbol{x}(t; \boldsymbol{x}_0 + \Delta\boldsymbol{x}_0, \boldsymbol{a}_{mod}) - \boldsymbol{x}(t; \boldsymbol{x}_0, \boldsymbol{a}_{ref}) \tag{26}$$

It is important to note that while this approach allows for unconstrained adjustments of the initial state, in practice, the uncertainty level of the available observations would limit the magnitude of these adjustments. By not imposing constraints on the initial state estimation, the results of this paper can be applied to scenarios with varying measurement accuracies. Furthermore, if the analysis suggests that a perturbation or model uncertainty should be included in the dynamics and the initial state adjustment is larger than allowed, imposing realistic constraints on the initial state estimation would reduce the absorption of the associated effect. As a result, larger post-fit residuals would be observed, reinforcing the conclusion that such aspects should be accounted for in the dynamical model.

Fig. 3 illustrates the two approaches schematically. In the first approach, both orbits start from the same common initial state, and their differences accumulate as the propagation progresses. In the second, the initial state of the reference orbit is used with the modified model to start an iterative process that yields a new, fitted orbit whose differences with the reference orbit are minimised.

The numerical implementation of both approaches relies on the free open-source TU Delft Astrodynamics Toolbox[1] (Tudat) [34,35], facilitating the reproducibility of the results presented in this paper. While the gravitational acceleration models detailed in Section 2.1 are included in Tudat's standard distribution, the software has been extended with acceleration models for free-molecular flow aerodynamics, solar radiation pressure, and planetary radiation pressure, implemented according to the equations provided in Sections 2.2–2.4.

The sensitivity of the ACS3 orbit to acceleration model modifications is evaluated using three complementary metrics: the root mean square (RMS) of the pre-fit residuals, the RMS of the post-fit residuals, and the magnitude of the maximum position adjustment required to minimise the residuals along the fitted arc. The RMS of pre-fit residuals offers a measure of the strength and influence of different perturbations and model uncertainties on the solar-sail dynamics, while their comparison with post-fit RMS residuals reveals the extent to which these effects can be absorbed by adjusting the initial state. Although pre-fit residuals provide valuable insights into the model's behaviour, the post-fit residuals guide the decision-making process. Depending on the model alteration under consideration, significant post-fit RMS residuals can indicate the need to include specific perturbations in the dynamics, suggest refining the acceleration model to address uncertainties and errors, or present opportunities for isolating and estimating parameters of interest. Conversely, negligible post-fit RMS residuals can uncover potential model simplifications without significant loss of accuracy, identify uncertain-

[1] https://docs.tudat.space/en/latest/, accessed August 08, 2024.

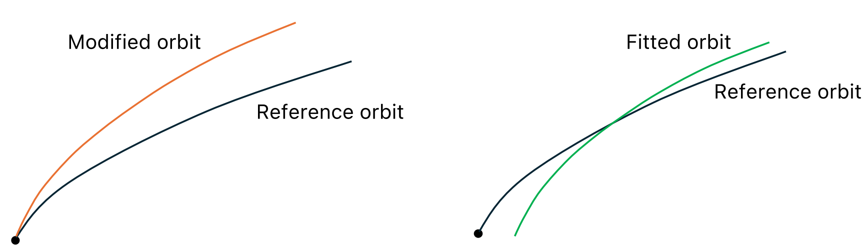

Fig. 3. Schematic representation of the propagation (left) and fitting (right) approaches.

ties and errors that can be absorbed through initial state adjustments, or identify parameters that may prove challenging to estimate. When the RMS of post-fit residuals falls below the observation noise level, the magnitude of the maximum required position adjustment along the fitted arc serves as an additional check. This metric helps to identify situations where an apparently good fit is achieved through observation adjustments that exceed realistic measurement uncertainties, indicating the fit may be unfeasible. The combined evaluation of these three metrics contributes to the estimation strategies of the ACS3 mission, guides the analysis of its flight data, and informs future solar-sail studies and missions.

4. Simulation setup

This section presents the simulation setup for the sensitivity analysis of the ACS3 solar-sail dynamics. Table 1 provides the values of the spacecraft properties and orbital parameters used as input for all simulations. This set of values, which remains unchanged throughout the study, includes the mass and sail area of ACS3, the simulation start epoch, and the corresponding sailcraft's initial orbital state. The simulation start epoch is set for November 1st, 2024, as it was originally expected that by this date, the commissioning phase of ACS3 would have been completed, with the sail fully deployed and operational. The initial state vector $\boldsymbol{x}_0$ is derived from the orbital elements representing a 1000 km altitude, circular, Sun-synchronous orbit with a 10:30 PM local time of the ascending node (LTAN). While this state vector is intended to represent ACS3 orbit after launch, the conclusions of the sensitivity analysis are independent of the exact initial state used. The choice of the simulation start epoch also does not influence the conclusions, as the initial state vector would be adjusted for any alternative date to ensure a 1000 km, Sun-synchronous orbit with a 10:30 PM LTAN. In addition to these common inputs, Table 2 presents the nominal values of the optical coefficients specific to the ACS3 solar sail [36]. These values are used in the reference acceleration model and are subject to variation in some modified acceleration models to evaluate their impact on the dynamics.

The following subsections detail the reference acceleration model and the modified acceleration models employed in both approaches of the sensitivity analysis.

Table 1
Constant simulation parameters.

Parameter	Symbol	Value
Sailcraft mass	m	16 kg
Sail area	A	80 m^2
Simulation start epoch	t_0	2024-11-01 00:00:00
Semi-major axis	a_0	7378136.3 m
Eccentricity	e_0	0.0
Inclination	i_0	99.4793 deg
Right ascension of ascending node	Ω_0	13.8328 deg
Argument of pericenter	ω_0	0.0 deg
True anomaly	θ_0	0.0 deg

Table 2
ACS3 optical coefficients.

Parameter	Frontside		Backside	
	Symbol	Value	Symbol	Value
Reflectivity[1]	$\tilde{r}_f$	0.90	$\tilde{r}_b$	0.43
Infrared Reflectivity[2]	$\tilde{r}_{f_{IR}}$	0.97	$\tilde{r}_{b_{IR}}$	0.40
Specularity	$\tilde{s}_f$	0.82	$\tilde{s}_b$	0.53
Non-Lambertian Coefficient	B_f	0.79	B_b	0.67
Emissivity	ε_f	0.03	ε_b	0.60

[1] These reflectivity values are used by the SRP and ARP models.
[2] These reflectivity values are used exclusively by the BBRP model.

4.1. Reference acceleration model

Table 3 presents the reference acceleration model, $\boldsymbol{a}_{ref}$, summarising the perturbations affecting the solar-sail dynamics and the nominal values of the parameters used in the perturbation models. Some of these parameters require further explanation:

- Accommodation coefficients, σ_n, σ_t: due to inconclusive evidence on particle reflection distribution and atomic oxygen adsorption at orbital altitudes higher than 500 km [41], σ_n and σ_t are both set to 0.8, consistent with other solar-sail studies [6,42,43].
- Speed ratio, s: at a 1000 km altitude, the atmospheric conditions are characterised by helium as the dominant species, with a mean molecular mass, m_a, of 3.94 kg/kmol and a translational temperature, T_∞, of 1000 K, as per the US76 Standard Atmosphere [44]. These values are used in Eq. (15) to compute the average thermal velocity, v_a. Combined with the sailcraft orbital speed of 7350 m/s for a 1000 km circular orbit, the value of v_a is used to obtain the speed ratio $s = 3.60$.
- Sail surface temperature, T_s: a thermal analysis is conducted considering the sailcraft's standby nadir-pointing attitude throughout its orbit. The orbit is divided into three phases: eclipse, back of the sail exposed to sunlight, and front of the sail exposed to sunlight, lasting 32.5%, 17%, and 50.5% of the orbital period, respectively. While the SRP alternately acts on the front and back of the sail, the PRP consistently acts on the back of the sail due to its nadir-pointing orientation. Assuming a uniform temperature distribution across the 2.115-micrometre thick sail [36], energy balance equations are formulated for each orbital phase:
  1. Eclipse: $(1-\tilde{r}_{b_{IR}})\,\bar{S}_{BBR} = (\varepsilon_f + \varepsilon_b)\,\sigma\, T_e^4$
  2. Back sunlit: $(1-\tilde{r}_{b_{IR}})\,\bar{S}_{BBR} + (1-\tilde{r}_b)(\cos\bar{\eta} + \bar{\Lambda}\,\phi)\,S_\oplus = (\varepsilon_f + \varepsilon_b)\,\sigma\, T_b^4$
  3. Front sunlit: $(1-\tilde{r}_{b_{IR}})\,\bar{S}_{BBR} + (1-\tilde{r}_f)\,S_\oplus \cos\bar{\eta} + (1-\tilde{r}_b)\,S_\oplus\,\bar{\Lambda}\,\phi = (\varepsilon_f + \varepsilon_b)\,\sigma\, T_f^4$

  In these equations, $\sigma = 5.670374419 \times 10^{-8}$ W/(m^2 K^4) is the Stefan-Boltzmann constant and the solar irradiance, $S_\oplus$, is set at 1361 W/m^2. The mean angle, $\bar{\eta}$, between the sail normal direction and the sunlight direction has values of 49 and 75 degrees when the front and the back of the sail are sunlit, respectively. These angles correspond to albedo phase functions, ϕ, of 0.6116 and 0.2630, respectively. In addition, the uniform albedo coefficient, $\bar{\Lambda}$, of 0.3259 and the uniform blackbody radiation flux, $\bar{S}_{BBR}$, of 234.723 W/m^2 are derived from surface-averaged ANGARA yearly maps. These maps, developed by Hyperschall Technologie Göttingen GmbH [45], use satellite data from the 1980s Earth Radiation Budget Experiment (ERBE) mission [46]. Using the energy balance equations, the sail surface temperature is computed as a weighted sum of the temperatures in each phase, where the weights correspond to the fraction of the orbital period spent in each phase:

$$T_s = 0.325\,T_e + 0.17\,T_b + 0.505\,T_f \tag{27}$$

- Atmospheric density, ρ: although not listed in Table 3, this property is required to compute the aerodynamic acceleration as specified in Eq. (12). The density value is obtained at each propagation step from the NRLMSISE-00 atmospheric density model [47], using indices of solar radio flux at 10.7 cm and geomagnetic activity relative to the 50th percentile retrieved from the Marshall Space Flight Center's forecast of August 2024.[2]
- Reference albedo coefficients, $\Lambda_{eq}, \Lambda_{pol}$, and blackbody radiation fluxes, $S_{BBR,eq}, S_{BBR,pol}$: the values of these parameters are determined through a sinusoidal least-squares fit to the ANGARA yearly

[2] https://www.nasa.gov/msfcsolar/archivedforecast, accessed August 08, 2024.

Table 3
Perturbations and nominal parameter values of the reference acceleration model.

Perturbation Type	Nominal Parameter Values	Equations
Earth gravity[1]	$l, m = 64$	(8)
Third-body gravity[2]		
Moon	$l, m = 2$	(10)
Sun, Venus, Jupiter	$l, m = 0$	(10)
Solid Earth Tides[3]	q = Sun, Moon; $l, m = 2$	(6)
Relativistic Effects	Schwarzschild corrections applied to Earth point mass gravity	(11)
Aerodynamics[4]	$\sigma_n, \sigma_t = 0.8$; $s = 3.60$; $T_\infty = 1000$ K; $T_s = 300$ K	(16)
Radiation Pressure[4,5]		
Solar	$S_\oplus = 1361.0$ W/m^2	(17)
Albedo	$S_\oplus = 1361.0$ W/m^2; $\Lambda_{eq} = 0.1854$; $\Lambda_{pol} = 0.6149$	(19), (21)
Blackbody	$S_{BBR,eq} = 264.6095$ W/m^2; $S_{BBR,pol} = 173.4356$ W/m^2	(19), (22)

[1] Earth gravitational parameter and spherical harmonics coefficients from Petit and Luzum [16] and Fecher et al. [37], respectively.
[2] Third bodies gravitational parameters from Park et al. [38]. Moon spherical harmonics coefficients from Goossens et al. [39].
[3] Love numbers $k_{2,0}$, $k_{2,1}$, $k_{2,2}$ from Petit and Luzum [16].
[4] Detailed explanations provided in the main text.
[5] Sail optical properties given in Table 2. Solar irradiance value from Kopp and Lean [40].

averaged albedo coefficient and blackbody radiation flux maps as a function of latitude.

4.2. Modified acceleration models

Table 4 presents an overview of the modified acceleration models, $\boldsymbol{a}_{mod}$, employed in the sensitivity analysis. Each modification is designed to investigate the impact of a specific perturbation or model parameter on the solar-sail dynamics. While most cases are self-explanatory from the table, several modifications to the reference acceleration model require additional explanation:

- Geopotential order variation: while the reference acceleration model uses a geopotential expansion up to degree and order 64 to balance accuracy and computational complexity, two higher-fidelity runs ($l, m = 128, 720$) are included to assess the influence of increased geopotential accuracy, with 720 being the maximum degree and order available in the GOCO05c gravity field model. Three lower-fidelity runs ($l, m = 32, 16, 8$) evaluate the impact of reduced accuracy.
- Density variation: two cases examine the effect of atmospheric density uncertainties on the solar-sail dynamics. The density values computed with the NRLMSISE-00 model are adjusted by $\pm 15\%$ at each propagation step. This range is based on estimates of upper atmospheric density model uncertainties, which typically fall between 10% and 15% [48]. Key factors contributing to these uncertainties include the varying solar extreme ultraviolet radiation, geomagnetic fluctuations, and localised changes in atmospheric conditions [49].
- Accommodation coefficients variation: two modifications to the accommodation coefficients are considered. The first case sets both normal and tangential coefficients to 1.0, representing a +25% variation from the nominal value and corresponding to fully diffusive particle reflection. The second case uses a value of 0.6 for both coefficients, representing a −25% variation from the nominal value and maintaining a quasi-specular reflection while exploring the impact of a lower particle reflection distribution.
- Sail temperature variation: the sensitivity to sail temperature is examined by considering two boundary conditions. The first condition corresponds to the minimum value of the sail temperature along the orbit, which occurs during eclipse at the poles, where only BBRP acts on the sail and the BBR flux is at its lowest. The second condition corresponds to the maximum value of the sail temperature along the orbit, which is achieved when all three radiation sources – Sun, blackbody, and albedo – illuminate the less reflective back of the sail, causing it to absorb more heat. The highest temperature in this scenario happens at the poles, where the albedo pressure is greatest, and at a sunlight incident angle of 60 degrees, the maximum angle for this scenario.
- Constant Sun-sailcraft distance: two cases are considered to evaluate the sensitivity of the solar radiation pressure to the instantaneous Sun-sailcraft distance, u. The first case assumes a constant value of 1 AU = 149597870700 m [16], while the second case sets the constant Sun-sailcraft distance equal to the arithmetic mean between the Sun-Earth distance at the simulation start and end epoch.
- Boundary cases for planetary radiation pressure: to assess the impact of variations in planetary radiation pressure, monthly values for the reference albedo coefficients and blackbody radiation fluxes are derived from sinusoidal least-squares fits to the ANGARA monthly maps as a function of latitude. From these fits, four distinct boundary cases are identified: the lowest average albedo coefficient (July), the highest average albedo coefficient (January), the lowest average blackbody radiation flux (March), and the highest average blackbody radiation flux (also July).
- Solar irradiance: two cases are considered to assess the sensitivity to variations in the nominal solar irradiance value of $S_\oplus = 1361$ W/m^2. The first case applies a 0.34% decrease, corresponding to the largest recorded short-term change in irradiance [40]. The second case applies a 0.12% increase, representing the average variation observed between solar minima and maxima [40].
- Optical coefficients variation: to address potential experimental errors in the testing of ACS3's film material, a one-sigma uncertainty of 10%[3] is considered for the optical coefficients listed in Table 2. The front infrared reflectivity is excluded from the analysis as it does not affect the sail acceleration due to the nadir-pointing attitude, where the blackbody radiation pressure acts only on the back of the sail.
- Attitude Error Model: The sailcraft orientation is defined by the sail normal direction pointing out from the back of the sail, $\hat{\boldsymbol{n}}$. Deviations from the nominal orientation are modelled with a rotation

[3] Uncertainty value taken from personal communication with J. Ho Kang, Advanced Materials and Processing Branch, NASA Langley Research Center, March 2024.

Table 4
Modified acceleration models employed in the sensitivity analysis.

Perturbation Source	Modification	Parameter Values
Geopotential	Order variation	l, m = 720, 128, 32, 16, 8
Third-body	Jupiter excluded	-
	Venus excluded	-
	Jupiter & Venus excluded	-
	Moon indirect oblation excluded	-
	Moon extended body contribution excluded	$l, m = 0$
Solid Tides	Excluded	-
Relativistic	Schwarzschild correction excluded	-
Aerodynamics	Density variation	$\pm 15\%$
	Accommodation coefficients variation	$\sigma_n, \sigma_t = 0.6, 1.0$
	Sail temperature variation	$T_s = 232\,\mathrm{K}, 374\,\mathrm{K}$
SRP	Constant Sun-sailcraft distance	u = 1AU, 148352576319.0875 m
	Ideal model	$b_1, b_3 = 0$; $b_2 = 1$
PRP	Ideal model	$\tilde{r}, \tilde{s} = 1$; G_{FND}, $G_{FT} = 0$
	Minimum AR configuration	$\Lambda_{\mathrm{eq}} = 0.2122$; $\Lambda_{\mathrm{pol}} = 0.5320$
	Maximum AR configuration	$\Lambda_{\mathrm{eq}} = 0.1917$; $\Lambda_{\mathrm{pol}} = 0.6416$
	Minimum BBR configuration	$S_{\mathrm{BBR,eq}} = 263.8755\ \mathrm{W/m^2}$; $S_{\mathrm{BBR,pol}} = 167.5518\ \mathrm{W/m^2}$
	Maximum BBR configuration	$S_{\mathrm{BBR,eq}} = 267.1935\ \mathrm{W/m^2}$; $S_{\mathrm{BBR,pol}} = 179.8487\ \mathrm{W/m^2}$
	Visible spectrum reflectivity for BBRP	-
SRP & PRP	Solar irradiance	$S_\oplus = 1356.4, 1362.6\ \mathrm{W/m^2}$
	Optical coefficient variation	$\pm 10\%$ to each coefficient in Table 2 excluding front infrared reflectivity
Spacecraft	Random attitude error	$\gamma = \mathcal{N}(0, 0.08°)$; $\delta = \mathcal{U}[0°, 360°)$ initial random seeds: 0, 15, 42
	Systematic attitude error	$\gamma = 0.08°$; $\delta = 0°, 15°, \ldots, 345°$

defined by a half-cone angle, γ, and a clock angle, δ. This rotation can be described using the Euler-Rodrigues rotation formula [50]:

$$\hat{\boldsymbol{n}}_{actual} = \hat{\boldsymbol{n}} \cos\gamma + (\hat{\boldsymbol{e}} \times \hat{\boldsymbol{n}}) \sin\gamma + \hat{\boldsymbol{e}}(\hat{\boldsymbol{e}} \cdot \hat{\boldsymbol{n}})(1 - \cos\gamma) \tag{28}$$

Here, $\hat{\boldsymbol{e}}$ is the rotation axis and is expressed in terms of two auxiliary vectors, $\hat{\boldsymbol{v}}_1$ and $\hat{\boldsymbol{v}}_2$:

$$\hat{\boldsymbol{v}}_1 = \frac{\boldsymbol{h} \times \hat{\boldsymbol{n}}}{\|\boldsymbol{h} \times \hat{\boldsymbol{n}}\|} \tag{29}$$

$$\hat{\boldsymbol{v}}_2 = \hat{\boldsymbol{n}} \times \hat{\boldsymbol{v}}_1 \tag{30}$$

$$\hat{\boldsymbol{e}} = \sin\delta\, \hat{\boldsymbol{v}}_2 - \cos\delta\, \hat{\boldsymbol{v}}_1 \tag{31}$$

where $\boldsymbol{h}$ is the angular momentum vector of the sailcraft orbit. The last term in the Eq. (28) vanishes as $\hat{\boldsymbol{e}} \cdot \hat{\boldsymbol{n}} = 0$, simplifying the actual unit normal vector to:

$$\hat{\boldsymbol{n}}_{actual} = \hat{\boldsymbol{n}} \cos\gamma + (\hat{\boldsymbol{v}}_1 \sin\delta + \hat{\boldsymbol{v}}_2 \cos\delta) \sin\gamma \tag{32}$$

A schematic representation of the attitude error model is shown in Fig. 4, which illustrates the relationship between the nominal and actual sailcraft orientations. The first three cases in the bottom row of Table 4 assess the sensitivity of the solar-sail dynamics to *random* attitude errors, each using a different seed number. In these cases, at each propagation step, half-cone angles are drawn from a half-normal distribution with a mean of zero and standard deviation of 0.08 degrees, while clock angles are drawn from a uniform distribution between 0 and 360 degrees. This standard deviation value corresponds to the absolute performance error of the attitude determination and control system of the ACS3 12U CubeSat, as specified by Nanoavionics,[4] and results in sailcraft attitude changes falling within the maximum turning rate of 0.5 degrees per second achievable by ACS3's reaction wheels. The remaining 24 cases evaluate *systematic* attitude errors using a fixed half-cone angle of 0.08 degrees and clock angles varying by 15-degree increments, thereby providing a comprehensive assessment of potential attitude biases across all directions.

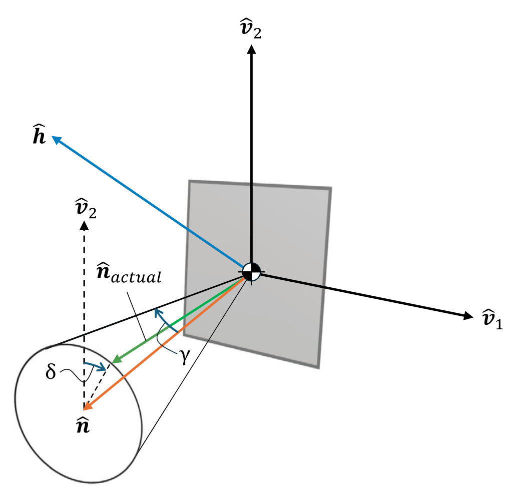

Fig. 4. Schematic representation of the attitude error model.

5. Results and discussion

This section presents the results of the sensitivity analysis of the ACS3 solar-sail dynamics to the modifications of the reference acceleration model detailed in Table 4. As discussed in Section 3, the impact of each modification is assessed based on the RMS of pre-fit and post-fit orbit residuals, as well as the maximum position adjustment required to minimise the residuals along the fitted arc.

For precise orbit determination, the accuracy of the acceleration model is crucial. If the model is insufficiently accurate, the least-squares

[4] https://nanoavionics.com/small-satellite-buses/12u-cubesat-nanosatellite-m12p/, accessed August 12, 2024.

algorithm may minimise errors induced by the model rather than errors in the measurements. Based on this consideration, the impact of acceleration model errors should be at least an order of magnitude smaller than that of measurement errors. For the discussion of the results, this paper assumes a one-sigma observation noise level of 10 metres on each Cartesian component. While such a noise level represents a realistic estimate for the ACS3 mission and reflects typical accuracies of onboard orbit solutions derived from GPS measurements, the results remain applicable to other noise levels, with implications scaling accordingly.

The discussion begins with the sensitivity of the ACS3 solar-sail dynamics to gravitational perturbations, followed by its sensitivity to non-gravitational perturbations, variations in the optical coefficients, and attitude errors. Tables A.1 through A.4 in Appendix A provide the numerical results of the sensitivity analysis for each acceleration model modification, complementing the graphical representations provided in the following subsections.

5.1. Gravitational perturbations

Fig. 5 illustrates how various gravitational perturbations influence the solar-sail dynamics. The geopotential model exhibits a clear trend of increasing impact as the degree and order of the expansion decrease. Higher-order potentials ($l, m = 720, 128$) show minimal deviations from the reference model, as both pre-fit and post-fit residuals remain well below the 1-meter model accuracy requirement. Lower-fidelity models, however, exhibit progressively larger residuals. The $l, m = 32$ expansion offers a potential model simplification, maintaining post-fit residuals near the 1-meter threshold and keeping position adjustments within the 10-meter observation uncertainty. In contrast, the $l, m = 16, 8$ cases show substantial orbital deviations, with residuals far exceeding the 10-meter observation noise level even after the initial state adjustment, indicating that such low-order models are inadequate for precise orbit determination.

The analysis of third-body effects reveals that Jupiter and Venus's contributions can be safely omitted from the dynamics without compromising accuracy – excluding either or both planets results in post-fit residuals three to four orders of magnitude below the model accuracy requirement. Similarly, neglecting the Moon's indirect oblation or its extended body contribution leads to post-fit residuals well below the 1-meter threshold, indicating that higher-order lunar perturbations are not essential in the acceleration model of the current mission scenario.

The exclusion of solid Earth tides results in post-fit residuals around ten metres, indicating that their effects should be included in the dynamical model of solar sails in LEO. In contrast, while neglecting the Schwarzschild relativistic correction initially produces considerable pre-fit residuals, post-fit values decrease by over three orders of magnitude. This behaviour is expected, as a minor adjustment to the initial state in the radial direction can largely absorb the impact of omitting this correction. The Schwarzschild term acts as a constant outward radial acceleration, and its exclusion can be seen as a change in the experienced central gravitational acceleration of the nominal orbit.

5.2. Non-gravitational perturbations

Fig. 6 presents the results of the sensitivity analysis for various modifications related to the aerodynamic, SRP, and PRP acceleration models. Atmospheric density variations significantly impact the sailcraft orbit, generating post-fit residuals exceeding 1 km. The symmetrical response of both pre-fit and post-fit residuals to $\pm 15\%$ variations indicates a linear performance between density changes and their influence on the orbital dynamics within the 7-day arc. This linearity allows the residuals to be scaled for different density uncertainty values within the considered range. Due to the multiplicative nature of the terms in Eq. (12), similar conclusions apply to uncertainties in other aerodynamic variables, such as the aerodynamic coefficients or the velocity relative to the atmosphere.

Modifications to the accommodation coefficients σ_n, σ_t also exhibit a linear behaviour over the 7-day arc, with post-fit residuals nearly double those observed for density variations. These results highlight the sensitivity of the solar-sail dynamics to atmospheric particle reflection

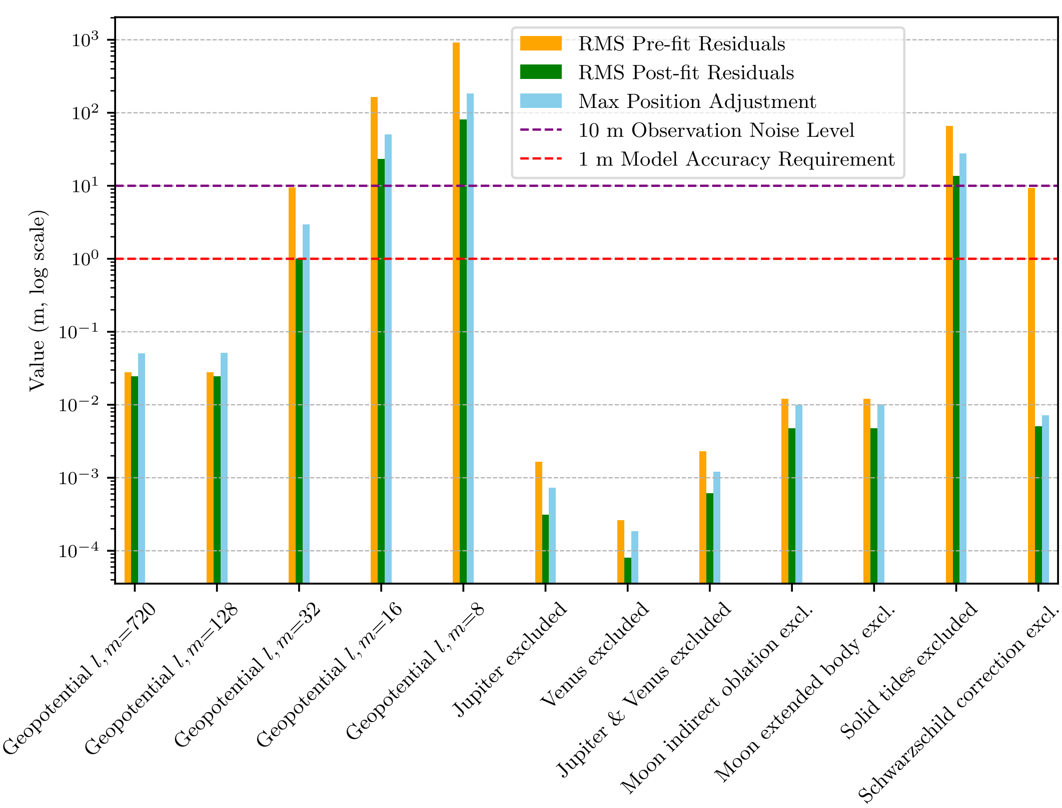

Fig. 5. Bar plot of the gravitational perturbations sensitivity results.

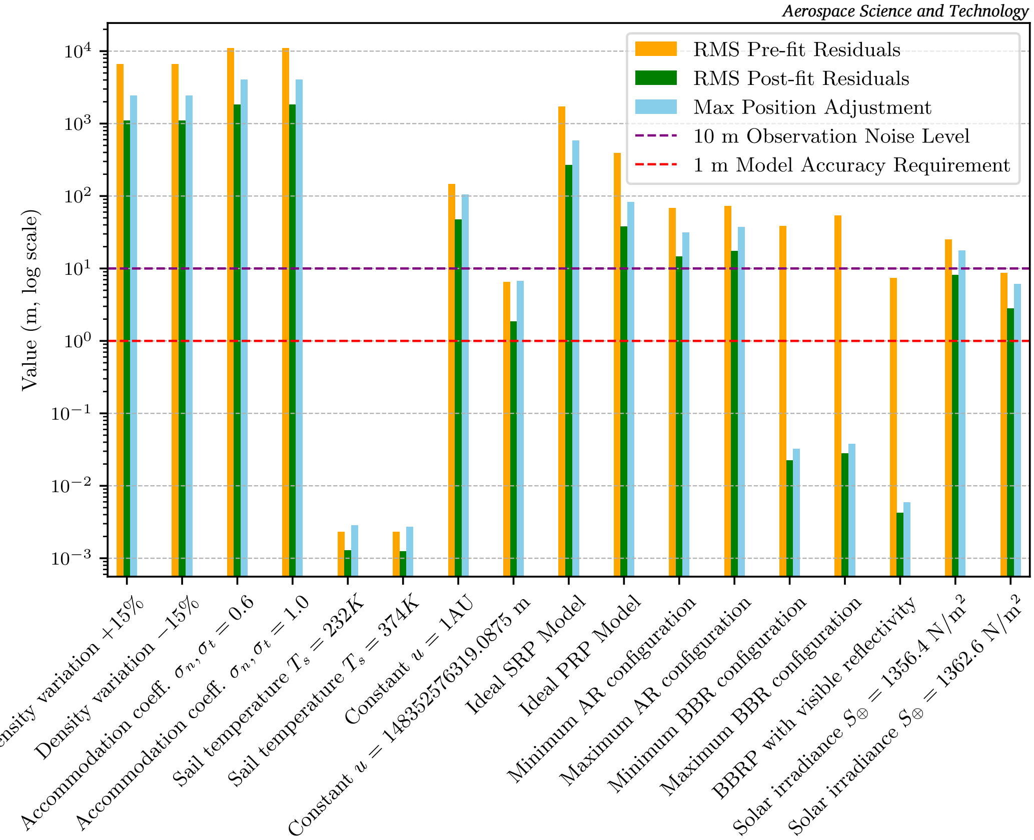

Fig. 6. Bar plot of the non-gravitational perturbations sensitivity results.

distribution and indicate the potential for accommodation coefficient estimation from flight data. In contrast, sail temperature variations show minimal impact on the orbit evolution, with post-fit residuals approximately three orders of magnitude below the model accuracy requirement.

The assumption of a constant Sun-sailcraft distance produces significant orbital deviations, with the 1 AU case showing larger effects than using the mean Earth-Sun distance over the simulation period. Both scenarios lead to post-fit residuals exceeding the 1-meter accuracy requirement, underlining the need to include the instantaneous Sun-sailcraft distance in the SRP acceleration model.

Simplifying the dynamics through the ideal SRP acceleration model results in post-fit residuals on the order of hundreds of meters, while using the ideal PRP acceleration model produces post-fit residuals in the tens of meters. This order-of-magnitude difference is also observed in the pre-fit values and reflects the relative strength of SRP and PRP accelerations in the ACS3 orbit. As the ideal models assume a perfect reflection of the radiation from the sail surface, the substantial deviations they produce emphasise the importance of accurately characterising the sail's optical properties and incorporating their effects in both SRP and PRP acceleration models.

Changes in the AR and BBR configurations result in a linear response of pre-fit and post-fit residuals within the 7-day arc. Despite producing variations of similar magnitude in the PRP acceleration, as evidenced by comparable pre-fit residuals, the post-fit values diverge significantly. Modifications in the reference albedo coefficients lead to post-fit residuals around ten meters, whereas changes in the reference blackbody radiation fluxes produce post-fit residuals approximately three orders of magnitude smaller. This divergence can be explained by the differing behaviour of the AR and BBR forces, even though both act radially when the sailcraft maintains a nadir-pointing attitude. Changes in albedo force are discontinuous due to the presence of eclipses, preventing initial state adjustments alone to compensate for them. The dependence of the albedo force on the illumination conditions of the Earth's visible surface may also complicate the absorption of associated model uncertainties. In contrast, the blackbody radiation force exhibits periodic, continuous changes, allowing them to be effectively absorbed by shifts in the initial radial position. This behaviour also appears when replacing infrared with visible reflectivity in the BBRP acceleration model, leading to a similar three-order magnitude difference between the pre-fit and post-fit residuals.

Finally, changes in the solar irradiance value also exhibit a linear behaviour over the 7-day arc. Post-fit residuals exceeding the 1-meter model accuracy requirement suggest that daily irradiance values should be used when available, with the lack of such data potentially posing a fundamental limitation on the model fidelity.

5.3. *Optical coefficients variations*

The results of the optical coefficients variations are presented in Fig. 7 and reveal different degrees of sensitivity across the various optical properties, with significant implications for both their observability and potential estimation strategies. The observed symmetry over the 7-day arc between positive and negative 10% variations of each coefficient enables the extension of the results to other uncertainty values of the optical coefficients within the original range. In this context, the surface roughness of the metal coating introduces local deviations in the sail optical properties that fall well within this studied interval. Therefore, the presented results can be used to gain insights into the impact of these deviations on the sail orbital evolution without the need to explicitly model microscale features in the solar-sail acceleration model.

Uncertainties in frontside reflectivity, $\tilde{r}_f$, and frontside specularity, $\tilde{s}_f$, have the largest impact on the orbit determination among the sail optical coefficients, with post-fit residuals well above the observation noise level. These parameters have a strong signature on the solar-sail dynamics, indicating they could be effectively estimated from flight data. Uncertainty in the backside non-Lambertian coefficient, B_b, leads to similarly large pre-fit residuals but smaller post-fit residuals. These results

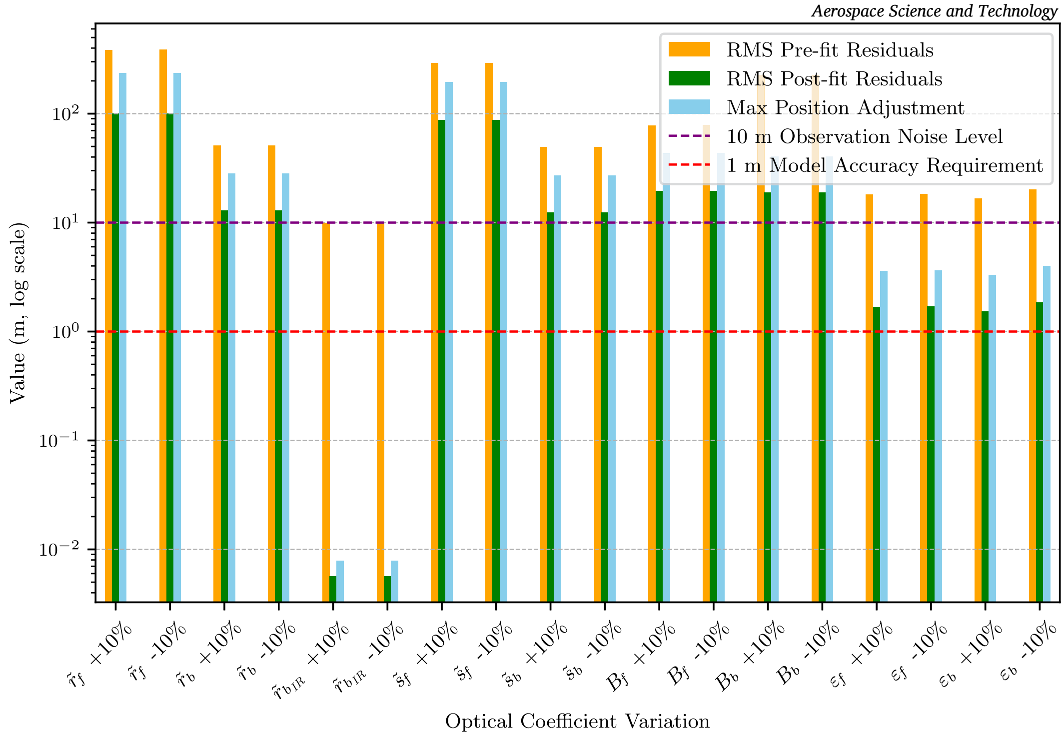

Fig. 7. Bar plot of the optical coefficients variations sensitivity results.

are consistent with the previously discussed behaviour, for which purely radial force changes, such as those caused by increasing or decreasing B_b, are effectively compensated for by adjustments in the initial radial position. In contrast, changes in $\tilde{r}_f$ and $\tilde{s}_f$ alter the SRP force in the radial, along-track, and cross-track directions, making their uncertainty more challenging to compensate for through initial state adjustments alone.

Variations of the frontside non-Lambertian coefficient, B_f, backside reflectivity, $\tilde{r}_b$, and backside specularity, $\tilde{s}_b$, demonstrate moderate effects on the orbit accuracy, though less pronounced than those of the frontside reflectivity and specularity. While four times smaller than the pre-fit values, their post-fit residuals still exceed the assumed 10-meter observation noise, suggesting that estimating their magnitude from flight data might be possible.

The uncertainty in the emissivity coefficients, ε_f and ε_b, leads to post-fit residuals that are one order of magnitude below the observation noise level, indicating that their signatures may be challenging to detect from the available observations. In contrast, the post-fit residuals for the infrared backside reflectivity, $\tilde{r}_{b_{IR}}$, are below one centimetre, suggesting it will be impossible to estimate its value from flight data. The three-order of magnitude drop between pre-fit and post-fit residuals occurs because changes in $\tilde{r}_{b_{IR}}$ only affect the BBR force, allowing the least-squares algorithm to effectively absorb these effects through initial state adjustments, as discussed earlier.

The observability of many of the optical coefficients, even for the relatively coarse orbital accuracy expected for the ACS3 mission, indicates that tracking data could potentially reduce the experimental uncertainty in these parameters. At the same time, the strong sensitivity of the solar-sail orbital dynamics to the modest uncertainties in the optical coefficients suggests that the optical solar-sail acceleration model may not fully capture the complex dynamics of solar sails.

5.4. Attitude errors

Fig. 8 illustrates the impact of attitude errors on the solar-sail orbital evolution. The first three cases, representing random attitude errors with different initial seeds, show consistent outcomes. While the comparison between pre-fit and post-fit residuals shows that the orbit determination process can mitigate random attitude errors of this small magnitude, the persistence of post-fit residuals slightly above the 1-meter threshold suggests that these errors may still have a limited impact on the overall accuracy of the orbit solution.

The analysis of systematic attitude errors across different clock angles reveals a clear pattern in the magnitude of orbital deviations, evident in both pre-fit and post-fit residuals. Cases corresponding to 0° and 180° clock angles exhibit the smallest deviations, while those at 90° and 270° clock angles show the largest deviations. All other cases show deviations between these extremes, with a gradual increase and decrease pattern observable as the clock angle changes. This pattern can be attributed to the direction of the normal vector offset relative to the sail orbit, with along-track offsets (90° and 270°) inducing larger cumulative position changes over time compared to out-of-plane offsets (0° and 180°).

Pre-fit residuals for the systematic attitude error cases span over an order of magnitude, demonstrating the varying impact that systematic attitude errors can have on the orbit accuracy. While post-fit residuals are consistently reduced from pre-fit values, the 1-meter model accuracy requirement is exceeded across all clock angles, with those near 0° and 180° just marginally exceeding the threshold. Additionally, the least-squares algorithm requires position adjustments larger than the 10-meter observation noise level to fit the observations for most clock angles, except near 0° and 180°.

The persistence of significant post-fit residuals for most systematic attitude errors indicates that these errors cannot be fully compensated by adjusting the initial state alone. Based on these findings, once mission data becomes available, several approaches could be considered to mitigate the impact of systematic attitude errors on accurate orbit determination. These approaches may include estimating empirical acceleration terms, implementing more sophisticated attitude models, or using *consider parameters* to assess the impact of attitude uncertainties on the overall orbit solution. Another approach could explore concurrent attitude and state estimation. However, accurate knowledge of the deployed sail geometry and centre of mass would be required for proper torque computation, or alternatively, a kinematic model would need to

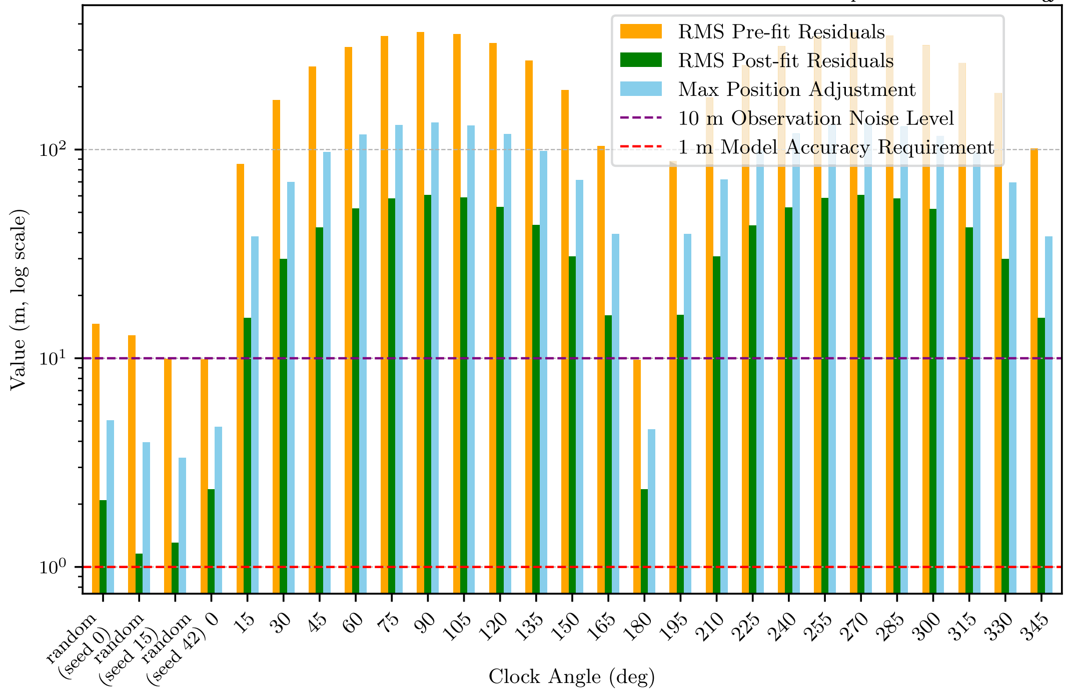

Fig. 8. Bar plot of the attitude errors sensitivity results.

be used for rotational motion alongside the dynamical model describing orbital motion. Overall, the observed pattern between the residuals and the clock angles offers valuable insight into which attitude error directions most significantly affect the sail orbital evolution, potentially guiding the focus of these mitigation strategies.

Systematic attitude errors can also be used to investigate the sensitivity to deformations in the sail surface, such as creases, crinkles, wrinkles, and asymmetric billowing. Since these deformations lead to deviations of local surface normals from their nominal flat-plate orientation, representing them through systematic attitude errors provides a way to assess their impact on the sail orbital evolution without requiring computationally expensive finite element modelling of the sail shape. The sensitivity of the orbit solution to even minor systematic attitude errors emphasises the critical importance of robust attitude determination and control systems for solar-sail missions. In addition to providing accurate knowledge of the sail orientation, these systems must be designed to actively compensate for unmodelled sail normal deviations and maintain commanded attitudes over time.

6. Conclusions

This paper has established a framework for identifying opportunities for dynamical model simplifications, evaluating the observability of solar-sail acceleration parameters, and quantifying the impact of model uncertainties and sail-attitude errors on solar-sail dynamics. For the one-sigma 10-meter observation noise level of the ACS3 mission and a seven-day arc, results have indicated that higher-order lunar perturbations, third-body effects from Jupiter and Venus, and relativistic corrections can be safely omitted from the dynamical model. Additionally, a geopotential expansion of degree and order 32 proves sufficiently accurate, and the BBRP acceleration can be modelled assuming visible reflectivity. In contrast, based on their significant post-fit signatures, the dynamics should include the effects of solid Earth tides, account for the instantaneous Sun-sailcraft distance in the SRP modelling, and employ optical models for both SRP and PRP accelerations.

The sensitivity analysis on the optical coefficients has shown different levels of observability, suggesting an iterative approach to parameter estimation once mission data becomes available. Initially, the estimation should focus on the frontside reflectivity and frontside specularity. These coefficients exhibit a strong influence on the dynamics and high observability, making them prime candidates for improving current solar-sail acceleration models. Properties with weaker dynamical signatures – the non-Lambertian coefficient, backside reflectivity, and backside specularity – could be estimated in subsequent iterations to refine the acceleration models further, although distinguishing their individual effects may prove challenging. The emissivity coefficients and infrared reflectivity show observability below the noise level and could, therefore, remain fixed or be treated as *consider parameters* within the orbit determination process. Overall, the pronounced signature of many of the optical coefficients on the solar-sail dynamics suggests that the data analysis may reveal deficiencies in the current solar-sail acceleration models.

The investigation of the model's robustness has revealed that the dynamics can absorb uncertainties in the sail's temperature and reference BBR fluxes, as well as random attitude errors of small magnitude. However, the model struggles to accommodate systematic attitude errors of similar magnitude and uncertainties in atmospheric density, accommodation coefficients, reference albedo coefficients, and solar irradiance. The uncertainties and errors that cannot be absorbed into ACS3's initial state present both challenges and opportunities. While they may complicate the estimation of optical coefficients from mission data, they could enable the investigation of additional physical phenomena through the orbit determination process. Of particular significance is the potential for estimating the accommodation coefficients, given their strong dynamical signature and the limited understanding of particle reflection distribution above 500 km altitude.

CRediT authorship contribution statement

Andrea Minervino Amodio: Conceptualization, Methodology, Software, Validation, Investigation, Writing – original draft, Writing – review & editing. **Pieter Visser:** Writing – review & editing, Supervision. **Jeannette Heiligers:** Writing – review & editing, Supervision, Funding acquisition.

Declaration of competing interest

The authors declare that they have no known competing financial interests or personal relationships that could have appeared to influence the work reported in this paper.

Acknowledgements

This work was funded by a Vidi Grant of the Dutch Research Council (NWO), Project Number 19690: SWEEP – Space Waste Elimination around Earth by Photon Propulsion. The authors would also like to thank Dr. Dominic Dirkx from the Department of Space Engineering at TU Delft for the several fruitful discussions on orbit determination aspects and on the use of the Tudat software.

Appendix A. Numerical results

Table A.1
Gravitational perturbations sensitivity results.

Perturbation	RMS Pre-fit Residuals (m)	RMS Post-fit Residuals (m)	Max Position Adjustment (m)
Geopotential $l, m = 720$	0.0278	0.0242	0.0504
Geopotential $l, m = 128$	0.0276	0.0242	0.0510
Geopotential $l, m = 32$	9.48	1.01	2.95
Geopotential $l, m = 16$	162.54	23.11	50.24
Geopotential $l, m = 8$	905.23	80.02	183.82
Jupiter excluded	0.00165	0.00031	0.000728
Venus excluded	0.000262	0.0000799	0.000183
Jupiter & Venus excluded	0.00231	0.000606	0.00121
Moon indirect oblation excluded	0.012	0.00476	0.01
Moon extended body excluded	0.012	0.00476	0.0101
Solid tides excluded	65.45	13.66	27.58
Schwarzschild correction excluded	9.26	0.00501	0.0071

Table A.2
Non-gravitational perturbations sensitivity results.

Perturbation	RMS Pre-fit Residuals (m)	RMS Post-fit Residuals (m)	Max Position Adjustment (m)
Density variation +15%	6593.89	1096.16	2414.57
Density variation −15%	6594.77	1096.11	2414.78
Accommodation coeff. $\sigma_n, \sigma_t = 0.6$	10987.57	1826.96	4024.60
Accommodation coeff. $\sigma_n, \sigma_t = 1.0$	10988.79	1826.83	4024.92
Sail temperature $T_s = 232K$	0.00232	0.00128	0.00283
Sail temperature $T_s = 374K$	0.00232	0.00124	0.00272
Constant u = 1AU	146.93	47.21	104.38
Constant u = 148352576319.0875 m	6.52	1.84	6.72
Ideal SRP Model	1700.21	267.27	584.74
Ideal PRP Model	392.64	37.92	81.79
Minimum AR configuration	68.54	14.59	31.22
Maximum AR configuration	72.80	17.43	37.36
Minimum BBR configuration	38.51	0.0223	0.0324
Maximum BBR configuration	54.07	0.0278	0.0376
BBRP with visible reflectivity	7.43	0.00424	0.0059
Solar irradiance $S_\oplus = 1356.4$ N/m^2	25.05	8.10	17.64
Solar irradiance $S_\oplus = 1362.6$ N/m^2	8.71	2.82	6.14

Table A.3
Optical coefficients variations sensitivity results.

Coefficient	Variation (%)	RMS Pre-fit Residuals (m)	RMS Post-fit Residuals (m)	Max Position Adjustment (m)
$\tilde{r}_f$	+10	383.80	100.01	236.32
$\tilde{r}_f$	-10	386.25	100.01	236.00
$\tilde{r}_b$	+10	51.07	12.92	28.26
$\tilde{r}_b$	-10	51.12	12.92	28.27
$\tilde{r}_{b_{IR}}$	+10	9.90	0.0057	0.0079
$\tilde{r}_{b_{IR}}$	-10	9.90	0.0057	0.0079
$\tilde{s}_f$	+10	291.07	87.24	194.53
$\tilde{s}_f$	-10	291.44	87.34	194.58
$\tilde{s}_b$	+10	49.41	12.35	27.06
$\tilde{s}_b$	-10	49.46	12.35	27.07
B_f	+10	78.16	19.62	43.37
B_f	-10	78.21	19.62	43.37
B_b	+10	226.89	18.86	40.42
B_b	-10	226.84	18.86	40.43
ε_f	+10	18.19	1.68	3.62
ε_f	-10	18.37	1.70	3.65
ε_b	+10	16.69	1.54	3.32
ε_b	-10	20.20	1.86	4.02

Table A.4
Attitude errors sensitivity results.

Clock Angle (deg)	RMS Pre-fit Residuals (m)	RMS Post-fit Residuals (m)	Max Position Adjustment (m)
random	14.65	2.09	5.03
random	12.88	1.16	3.95
random	9.91	1.31	3.34
0	9.90	2.36	4.70
15	85.08	15.58	38.38
30	173.00	29.95	70.07
45	249.80	42.45	97.21
60	310.20	52.17	117.95
75	349.97	58.43	130.84
90	366.11	60.76	134.89
105	357.22	58.93	130.37
120	323.61	53.03	118.51
135	267.42	43.44	98.39
150	192.52	30.83	71.39
165	104.14	16.09	39.32
180	9.84	2.36	4.56
195	87.94	16.11	39.48
210	177.53	30.77	71.81
225	254.46	43.30	99.02
240	313.42	52.80	119.25
255	350.55	58.64	131.19
270	363.57	60.45	134.10
285	351.89	58.15	128.82
300	316.61	51.96	116.32
315	260.30	42.32	96.07
330	186.82	29.91	69.47
345	101.07	15.61	38.34

Data availability

Data will be made available on request.

References

[1] P. Zhao, C. Wu, Y. Li, Design and application of solar sailing: A review on key technologies, Chin. J. Aeronaut. 36 (2023) 125–144.
[2] M. Macdonald, C. McInnes, Solar sail science mission applications and advancement, Adv. Space Res. 48 (2011) 1702–1716.
[3] D.A. Spencer, L. Johnson, A.C. Long, Solar sailing technology challenges, Aerosp. Sci. Technol. 93 (2019).
[4] D.A. Spencer, B. Betts, J.M. Bellardo, A. Diaz, B. Plante, J.R. Mansell, The Lightsail 2 solar sailing technology demonstration, Adv. Space Res. 67 (2021) 2878–2889.
[5] W.K. Wilkie, J.M. Fernandez, O.R. Stohlman, N.R. Schneider, G.D. Dean, J. Ho Kang, J.E. Warren, S.M. Cook, P.L. Brown, T.C. Denkins, S.D. Horner, E.D. Tapio, M. Straubel, M. Richter, J. Heiligers, Overview of the NASA Advanced Composite Solar Sail System (ACS3) technology demonstration project, in: AIAA Scitech 2021 Forum, 2021.
[6] L. Carzana, P. Visser, J. Heiligers, Locally optimal control laws for earth-bound solar sailing with atmospheric drag, Aerosp. Sci. Technol. 127 (2022) 107666.
[7] A. Barles, M. Ceriotti, F. Ciampa, L. Felicetti, An optimal steering law for sailing with solar and planetary radiation pressure, Aerosp. Sci. Technol. 118 (2021).
[8] A. De Iuliis, F. Ciampa, L. Felicetti, M. Ceriotti, Sailing with solar and planetary radiation pressure, Adv. Space Res. 67 (2021) 2795–2811.
[9] M. Macdonald, C. McInnes, Analytical control laws for planet-centered solar sailing, J. Guid. Control Dyn. 28 (2005) 1038–1048.
[10] M. Macdonald, C. McInnes, Geosail: Exploring the magnetosphere using a low-cost solar sail, Acta Astronaut. 59 (2006) 757–767.
[11] M. Macdonald, C. McInnes, Realistic earth escape strategies for solar sailing, J. Guid. Control Dyn. 28 (2005) 315–323.
[12] B. Dharmadasa, F. Lopez Jimenez, Modeling the effect of creases in an unfolding membrane, in: AIAA Scitech 2021 Forum, 2021.
[13] G. Vulpetti, D. Apponi, X. Zeng, C. Circi, Wrinkling analysis of solar-photon sails, Adv. Space Res. 67 (2021) 2669–2687.
[14] J. Wang, Z. Cheng, G. He, H. Yuan, Uncertainty characterization of solar sail thrust with a multiscale modeling method, Adv. Space Res. (2025).
[15] O. Montenbruck, E. Gill, Satellite orbits: Models, methods and applications, 1st ed., Springer, Berlin, Heidelberg, 2000.
[16] G. Petit, B. Luzum, IERS conventions (2010), IERS Technical Note 36, 2010.
[17] T. Moyer, Mathematical formulation of the Double-Precision Orbit Determination Program (DPODP), Technical Report, Jet Propulsion Laboratory, 1971.
[18] K. Roh, S. Kopeikin, J. Cho, Numerical simulation of the post-newtonian equations of motion for the near earth satellite with an application to the lares satellite, Adv. Space Res. 58 (2016) 2255–2268.
[19] J.R. Wertz, W.J. Larson, D. Kirkpatrick, D. Klungle, Space mission analysis and design, 3rd ed., Springer, Dordrecht, 1999.
[20] D. Dirkx, E. Mooij, Conceptual shape optimization of entry vehicles: Applied to capsules and winged fuselage vehicles, Springer International Publishing, 2017.
[21] E.D. Knechtel, W.C. Pitts, Normal and tangential momentum accommodation for earth satellite conditions, Astronaut. Acta 18 (1973) 171–184.
[22] S. Schaaf, P. Chambre, Flow of rarefied gases, High Speed Aerodynamics and Jet Propulsion, Princeton University Press, Princeton, NJ, 1958.
[23] L. Sentman, Free molecule flow theory and its application to the determination of aerodynamic forces, Technical Report LMSC-448514, Lockheed Missile and Space Co., Sunnyvale, CA, 1961.
[24] R. Schamberg, A new analytic representation of surface interaction for hyperthermal free molecule flow, Technical Report RM-2313, RAND Corp, Santa Monica, CA, 1959.
[25] J.A. Storch, Aerodynamic disturbances on spacecraft in free-molecular flow, Technical Report TR-2003(3397)-1, The Aerospace Corporation, 2003.
[26] P. Hughes, Spacecraft attitude dynamics, Dover Publications Inc., New York, 2004.
[27] C.R. McInnes, Solar sailing: Technology, dynamics and mission applications, 1st ed., Springer, London, 1999.
[28] L. Carzana, P. Visser, J. Heiligers, A new model for the planetary radiation pressure acceleration for optical solar sails, in: 6th International Symposium on Space Sailing (ISSS 2023), New York, USA, 2023, pp. 97–104.
[29] L. Carzana, P. Visser, J. Heiligers, A new model for the planetary radiation pressure acceleration for solar sails, J. Guid. Control Dyn. 47 (2024) 1674–1687.
[30] S. Tragesser, J. Longuski, Modeling issues concerning motion of the Saturnian satellites, J. Astronaut. Sci. 47 (1999) 275–294.
[31] L. Iorio, V. Lainey, The Lense-Thirring effect in the Jovian system of the Galilean satellites and its measurability, Int. J. Mod. Phys. D 14 (2005) 2039–2049.
[32] L. Beauvalet, V. Lainey, J.-E. Arlot, R. Binzel, Dynamical parameter determinations in Pluto's system. Expected constraints from the new horizons mission to Pluto, Astron. Astrophys. 540 (2012) A65.
[33] D. Dirkx, V. Lainey, L. Gurvits, P. Visser, Dynamical modelling of the Galilean moons for the JUICE mission, Planet. Space Sci. 134 (2016) 82–95.
[34] D. Dirkx, E. Mooij, B. Root, Propagation and estimation of the dynamical behaviour of gravitationally interacting rigid bodies, Astrophys. Space Sci. 364 (2019) 1–22.
[35] D. Dirkx, M. Fayolle, G. Garrett, M. Avillez, K. Cowan, S. Cowan, J. Encarnacao, C. Fortuny Lombrana, J. Gaffarel, J. Hener, et al., The open-source astrodynamics Tudatpy software – Overview for planetary mission design and science analysis, Europlanet Science Congress 2022 (16) (2022).
[36] W.K. Wilkie, The NASA Advanced Composite Solar Sail System (ACS3) flight demonstration: A technology pathfinder for practical smallsat solar sailing, in: 35th Annual Small Satellite Conference, Logan, Utah, USA, 2021, pp. 1–15.
[37] T. Fecher, R. Pail, T. Gruber, the GOCO Consortium, GOCO05c: A new combined gravity field model based on full normal equations and regionally varying weighting, Surv. Geophys. 38 (2017) 571–590.
[38] R. Park, W. Folkner, J. Williams, D. Boggs, The JPL planetary and lunar ephemerides DE440 and DE441, Astron. J. 161 (2021) 105.

[39] S. Goossens, F.G. Lemoine, T.J. Sabaka, J.B. Nicholas, E. Mazarico, D.D. Rowlands, B.D. Loomis, D.S. Chinn, G.A. Neumann, D.E. Smith, M.T. Zuber, A global degree and order 1200 model of the lunar gravity field using GRAIL mission data, in: 47th Annual Lunar and Planetary Science Conference, Lunar and Planetary Science Conference, 2016, p. 1484.

[40] G. Kopp, J. Lean, A new, lower value of total solar irradiance: Evidence and climate significance, Geophys. Res. Lett. 38 (2011).

[41] A. Walker, P. Mehta, J. Koller, Drag coefficient model using the Cercignani–Lampis–Lord gas-surface interaction model, J. Spacecr. Rockets 51 (2014).

[42] G. Mengali, A.A. Quarta, Near-optimal solar-sail orbit-raising from low Earth orbit, J. Spacecr. Rockets 42 (2005) 954–958.

[43] V. Stolbunov, M. Ceriotti, C. Colombo, C.R. McInnes, Optimal law for inclination change in an atmosphere through solar sailing, J. Guid. Control Dyn. 36 (2013) 1310–1323.

[44] US76, U.S. Standard Atmosphere, 1976, Technical Report, U.S. Government Printing Office, Washington, D.C., 1976.

[45] B. Fritsche, M. Ivanov, A. Kashkovsky, G. Koppenwallner, A. Kudryavtsev, U. Voskoboinikov, G. Zhukova, Radiation pressure forces on complex spacecraft, final report, Technical Report ESOC contract 11908, European Space Operations Centre (ESOC), Darmstadt, Germany, 1998.

[46] E. Doornbos, S. Bruinsma, B. Fritsche, G. Koppenwallner, P. Visser, J. Van Den IJssel, J.D.T. de Encarnação, GOCE+ theme 3: Air density and wind retrieval using GOCE data, Algorithm Theoretical Basis Document ESTEC contract 4000102847, European Space Research and Technology Centre (ESTEC), 2014.

[47] J.M. Picone, A.E. Hedin, D.P. Drob, A.C. Aikin, NRLMSISE-00 empirical model of the atmosphere: Statistical comparison and preliminary validation, J. Geophys. Res. 107 (2002).

[48] D. Vallado, D. Finkleman, A critical assessment of satellite drag and atmospheric density modeling, Acta Astronaut. 95 (2014) 141–165.

[49] D. Mostaza Prieto, B.P. Graziano, P.C.E. Roberts, Spacecraft drag modelling, Prog. Aerosp. Sci. 64 (2014) 56–65.

[50] J.E. Mebius, Derivation of the Euler-Rodrigues formula for three-dimensional rotations from the general formula for four-dimensional rotations, Mathematics (2007).